Electronic Supporting Information

Waste is the Best: *End-of-Life* Lithium Ion Battery-derived Ultra-active Ni^{3+}-Enriched β-$Ni(OH)_2$ for Electrocatalytic Oxygen Evolution Reaction

Hiren Jungi, [a,b] Arun Karmakar, [b,c] Subrata Kundu, [b,c]* Joyee Mitra [a,b]*

[a] Inorganic Materials & Catalysis Division, CSIR-Central Salt & Marine Chemicals Research Institute, Gijubhai Badheka Marg, Bhavnagar-364002, Gujarat, India.

[b] Academy of Scientific and Innovative Research (AcSIR), AcSIR Headquarters, CSIR-HRDC Campus, Sector -19, Kamla Nehru Nagar, Ghaziabad-201002, U.P. India.

[c] Electrochemical Process Engineering (EPE) Division, CSIR-CECRI, Karaikudi, Tamil Nadu-630003.

Email: skundu@cecri.res.in, kundu.subrata@gmail.com (SK)

joyeemitra@csmcri.res.in, joyeemitra@gmail.com (JM)

No. of Pages: 19 (S1-S19)

No. of Figures: 18 (Figure S1 – S18)

No. of Tables: 3

Index **Page no.**

1. Experimental section

Chemicals & Materials:

The spent lithium-ion batteries were purchased from the local market in Bhavnagar. Deionized water was used for dilution and to prepare all the solutions. All the reagents used were of analytical grade. Dimethylglyoxime (99%), sodium hydroxide (96%), and hydrochloric acid (37%) used in this paper were purchased from CDH Pvt. Ltd.

Separation of nickel from the leached liquor of NMC-type batteries and precipitation of $Ni(DMG)_2$ complex

Nickel can be selectively recovered from the leached liquor of end-of-life NMC-type lithium ion batteries (LIBs) as $Ni(DMG)_2$ complex.[1] Dropwise addition of dimethyl glyoxime (DMG) solution in ethanol (2.25 equiv.) to the acidic leached liquor (pH ~ 3.4) of LIBs results in the precipitation of red-colored $Ni(DMG)_2$ complex. The solution was then stirred for a further 30 mins at room temperature (**Scheme 1**). The other metals are not precipitated under the reaction conditions.[2] The precipitated $Ni(DMG)_2$ complex was washed with deionized water and dried in air at 70 °C for 12 hr.

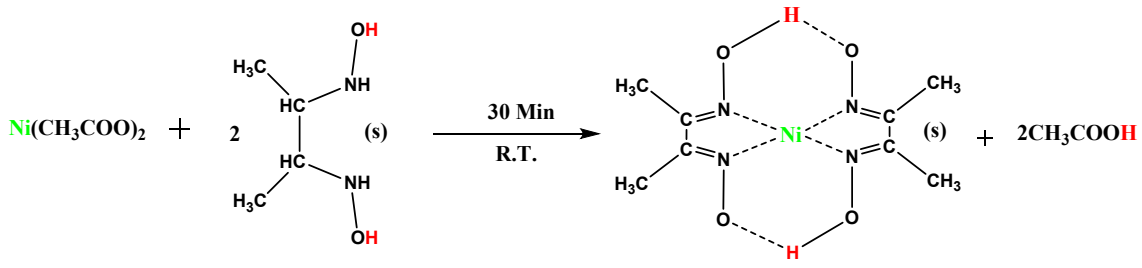

Scheme 1: Preparation of $Ni(DMG)_2$ complex

Recovery of DMG from $Ni(DMG)_2$ complex and the Synthesis of β-$Ni(OH)_2$

DMG can be recovered from the precipitated $Ni(DMG)_2$ complex by the addition of 7 % HCl followed by stirring for 10 min at room temperature. Ni^{2+} leaches out as $NiCl_2$ and the insoluble DMG precipitates out. The DMG was collected by filtration and thoroughly washed with deionized water. The phase purity of the recovered DMG was ascertained from PXRD analysis (**Figure S7)**. The recovered DMG can be reused for the selective precipitation of Ni from LIBs.

$$Ni(C_4H_7N_2O_2)_2 + 2HCl \longrightarrow NiCl_2 + 2C_4H_8N_2O_2 \quad pH \sim 1.1 \quad (1)$$

β-$Ni(OH)_2$ was synthesized from the leached light green colored $NiCl_2$ solution obtained during the recovery of DMG, by the addition of NaOH. The initial pH of ~ 1.1 was slowly raised to ~ 11 by the gradual addition of saturated aq. NaOH solution. β-$Ni(OH)_2$ forms as a green colored precipitate. The precipitate was aged in the solution for a further 1 h, after which it was recovered from the alkaline NaOH solution by centrifugation. The precipitate was washed thoroughly with a basic solution three to four times to remove the residual DMG followed by washing with deionized water. The obtained β-$Ni(OH)_2$ was air dried at 60 °C for 24 hr.

$$NiCl_2 + 2NaOH \longrightarrow \beta\text{-}Ni(OH)_2\downarrow + 2NaCl \quad pH \sim 11.0 \quad (2)$$

Experimental details for Electrocatalytic Oxygen Evolution Reaction

The β-$Ni(OH)_2$, $Ni(DMG)_2$ were applied for alkaline water oxidation reaction in 'Fe free' 1 M KOH solution at ambient conditions. All the electrochemical studies have been carried out using conventional three electrode system. Here Hg/HgO and Graphite rode have been used as reference and counter electrode respectively. Backward LSVs have been used to check the oxygen evolution reaction (OER) activity to nullify the interference of oxidation peaks that usually arise in the potential range of 1.25-1.35 V vs RHE in case of forward CV. A scan rate of 5 mV/sec has been using to obtain all the LSV information. Incessant rapid sweeping

through accelerated degradation (AD) studies at a very high sweep rate of 200 mVs^{-1} for 500 cycles were carried out in the same alkaline environment. The electrochemical impedance studies were carried out in the frequency range of 0.1 Hz to 100 kHz with an overpotential of 250 mV. All the electrodes have been fabricated *via* simple drop-casting methods and the catalyst ink were prepared by mixing 3 mg of catalyst powder in a mixture of 750 μL of DI water, 200 μL of ethanol and 50 μL of Nafion solution followed by ultrasonication for 15 minutes. 34.5 μL of as prepared ink solution was drop-cast over the carbon cloth previously washed with ethanol acetone mixture. The dried catalysts over carbon cloth as conducting substrate have been used as catalysts to study OER using 1 M KOH as the electrolyte.

2. Characterization:

The crystallinity of the cathode material obtained from the spent lithium ion batteries were were investigated by X-ray diffracting pattern (XRD; RIGAKU, MiniFlexII) using Cu Kα radiation (α=1.54 Å). The surface morphology of the catalyst was characterized by scanning electron microscopy (FE-SEM; JEOL JEM-2010) with the energy dispersive system EDX. The in-depth analysis confirms by high-resolution transmission electron microscopy (HR-TEM; JEOL, JEM 2100 instrument). The specific surface area was determined by using Brunauer-Emmett-Teller (BET)(Quantachrome; autosorb iQ-MP/XR). The surface chemical nature of elements was examined by X-ray photoelectron microscopy (XPS; Thermo-Scientific, NEXSA) using an X-ray source as Al Kα. The decomposition temperature of the catalyst was studied by thermal gravimetric analysis (TGA; NETZ5CH; DMA 242 E Artemis). The characteristic band was analyzed by Fourier transform infrared spectroscopy using KBr pellets as internal standard (FTIR; Perkin–Elmer GX FTIR spectrometer). The element analysis of was studied by Inductively coupled plasma mass spectrometry (ICP-MS; ThermoFisher; iCAP

RQ). Surface charge on catalysis was examined by Zeta Potential (MALVERN; ZETASIZER; Nano-Z5) and Raman spectroscopy was done (HORIBA, OLYMPUS BX41).

Cathode material from NMC-type End-of-life Lithium ion battery

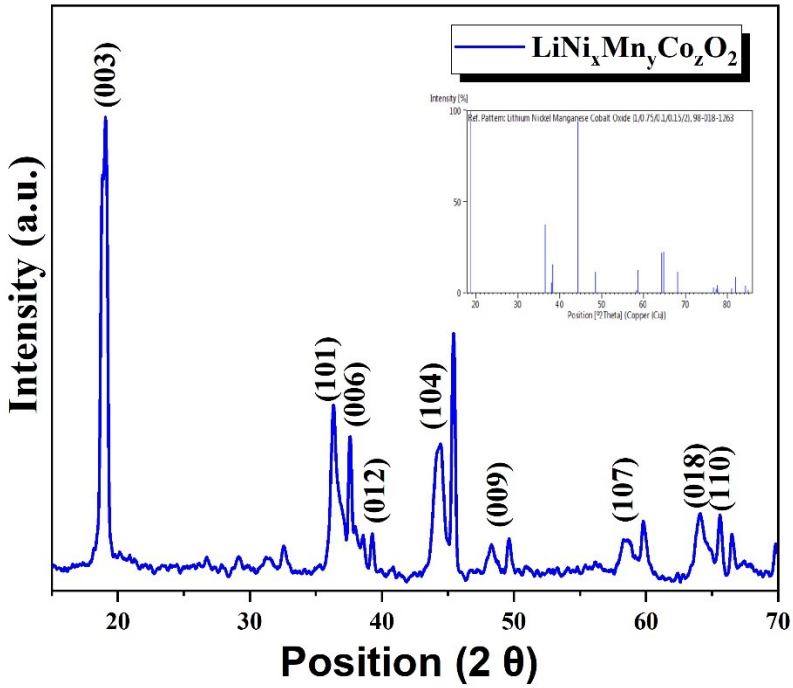

Figure S1. PXRD pattern of cathode material from the end-of-life NMC-type lithium ion batteries. Inset shows the PXRD pattern of lithium nickel manganese cobalt oxide.

Characterization Data of $Ni(DMG)_2$ complex:

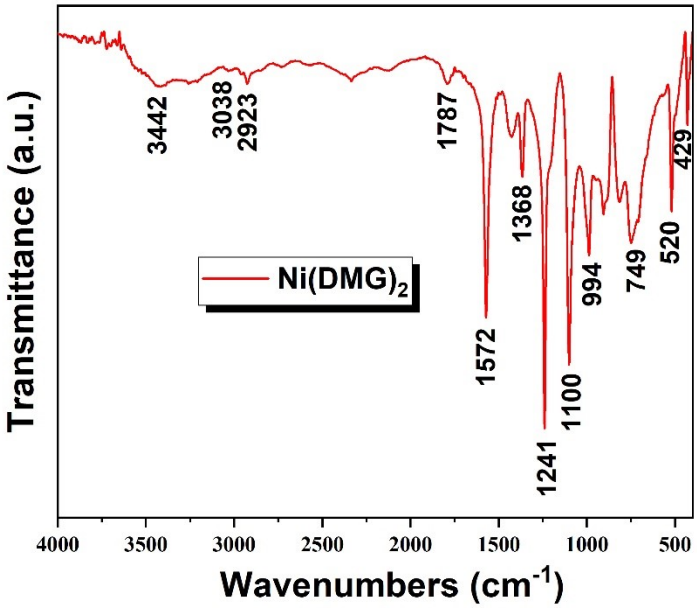

Figure S2. FTIR spectrum of $Ni(DMG)_2$ complex obtained by the selective recovery of Ni from the spent NMC-type LIBs.

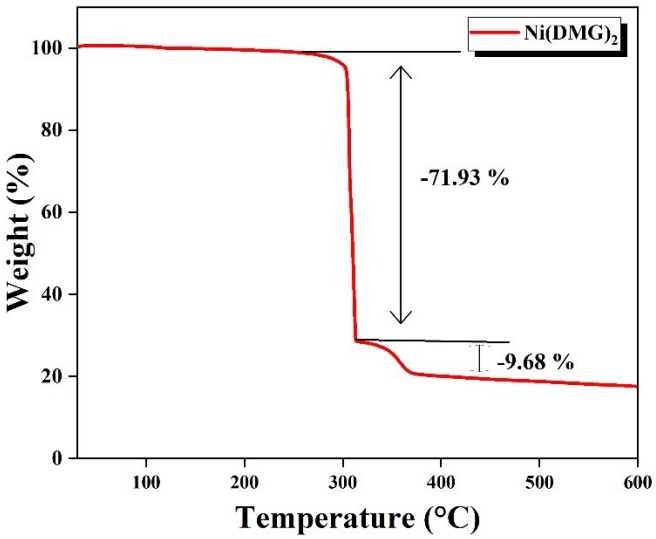

Figure S3. TGA of $Ni(DMG)_2$ complex obtained by the selective recovery of Ni from the spent NMC-type LIBs.

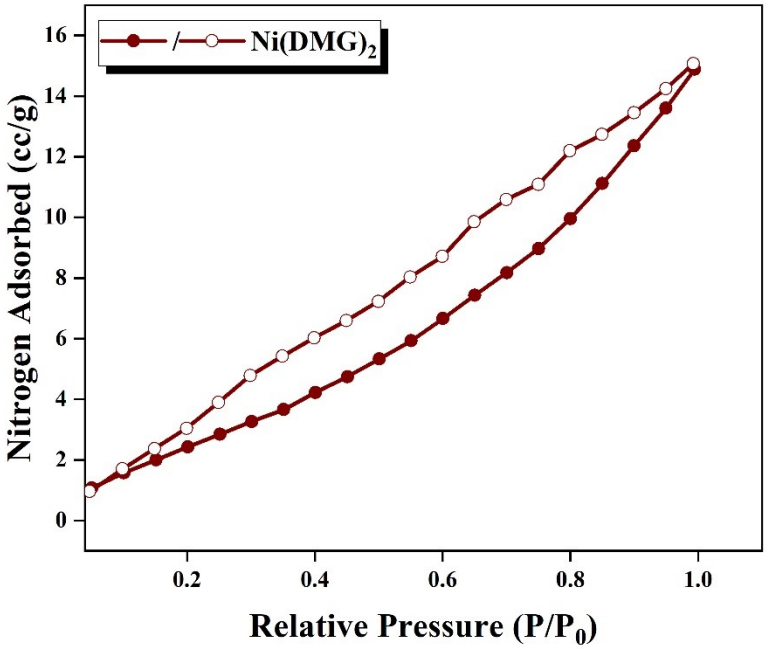

Figure S4. N_2 adsorption-desorption isotherm of $Ni(DMG)_2$ complex obtained by the selective recovery of Ni from the spent NMC-type LIBs.

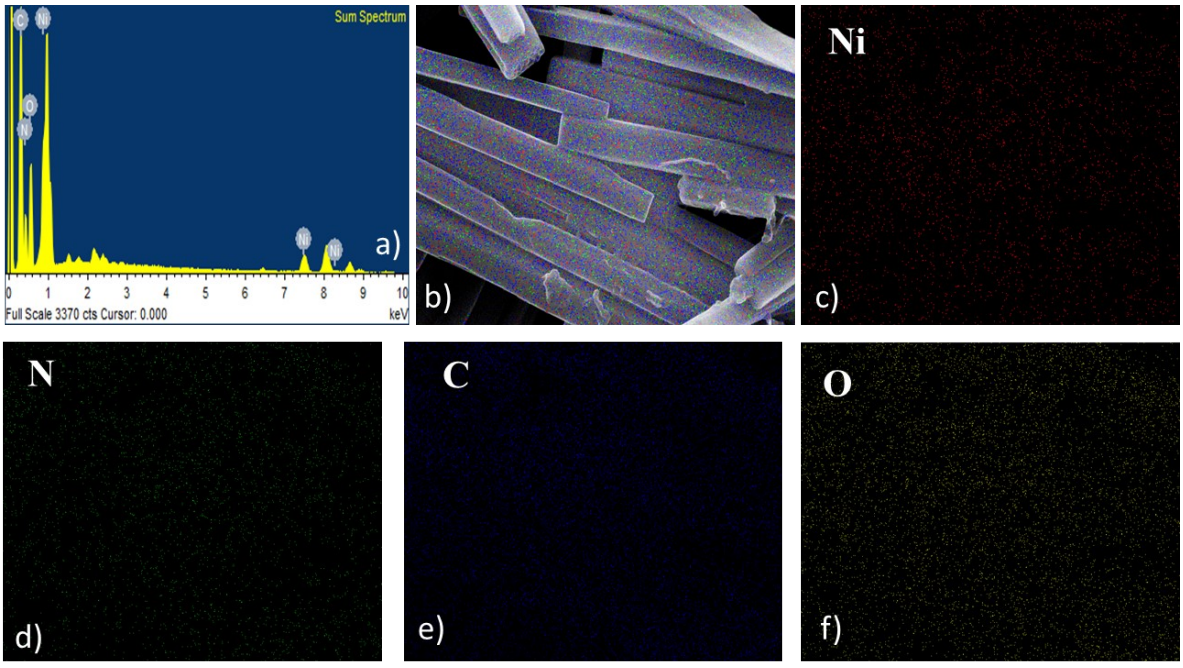

Figure S5. a) SEM-EDX of $Ni(DMG)_2$ complex showing the presence of elements Ni, C, O and N. FESEM elemental mapping of $Ni(DMG)_2$ is presented in b) – f), where b) represents the merged data of the elements while c) to f) maps the elements Ni, N, C and O respectively.

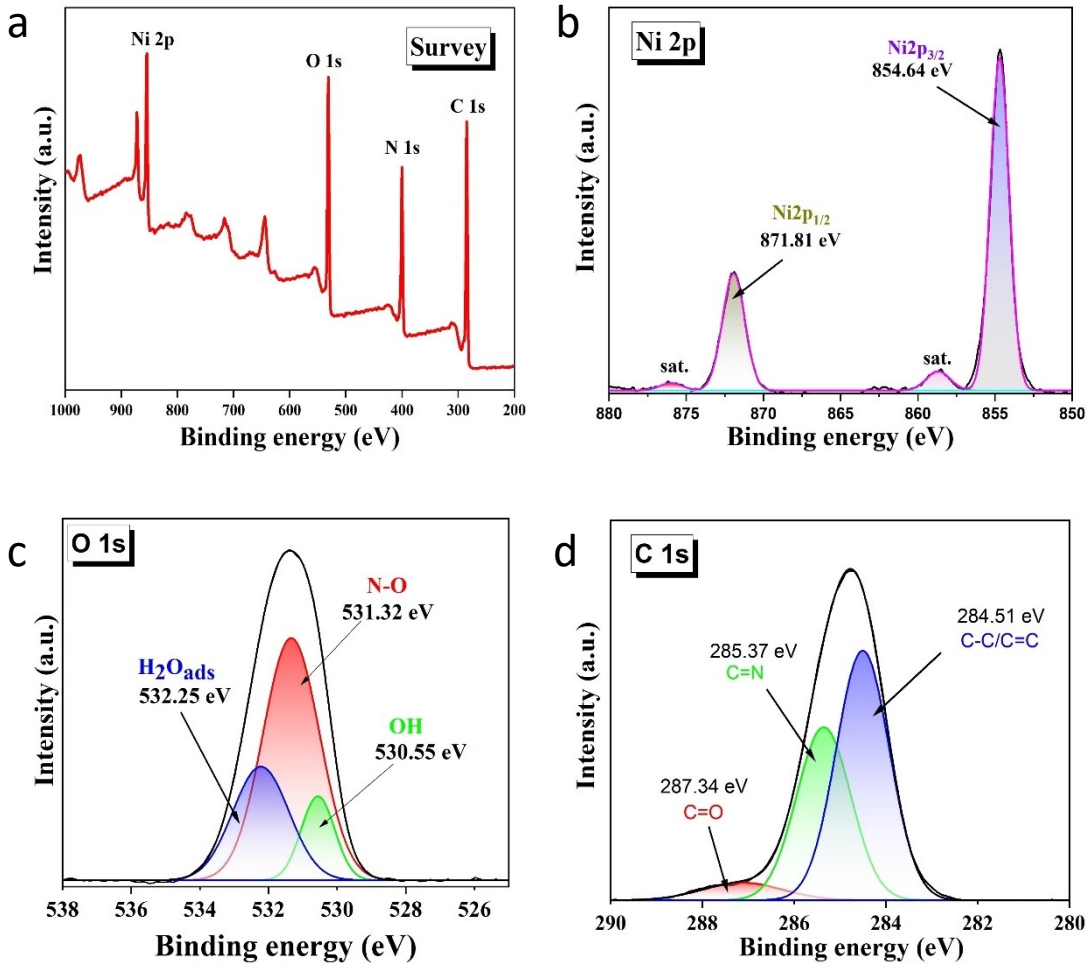

Figure S6. a) XPS survey spectrum of $Ni(DMG)_2$. O 1s and C 1s XPS spectra of $Ni(DMG)_2$ are presented as b) and c) respectively.

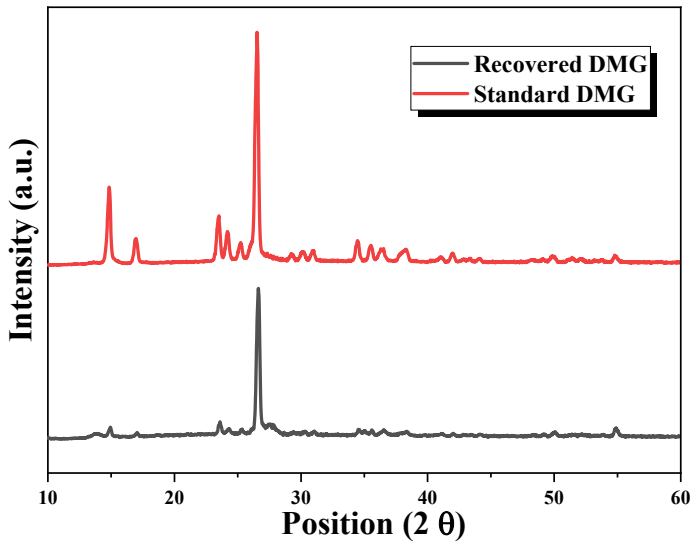

Figure S7. PXRD data of recovered DMG.

Characterization Data of β-Ni(OH)$_2$ complex:

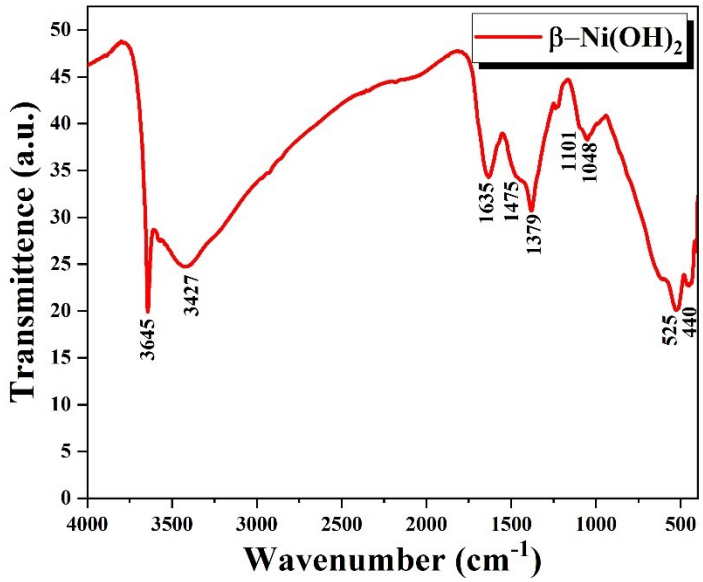

Figure S8. FTIR spectrum of end-of-life LIB-derived **β-Ni(OH)$_2$**

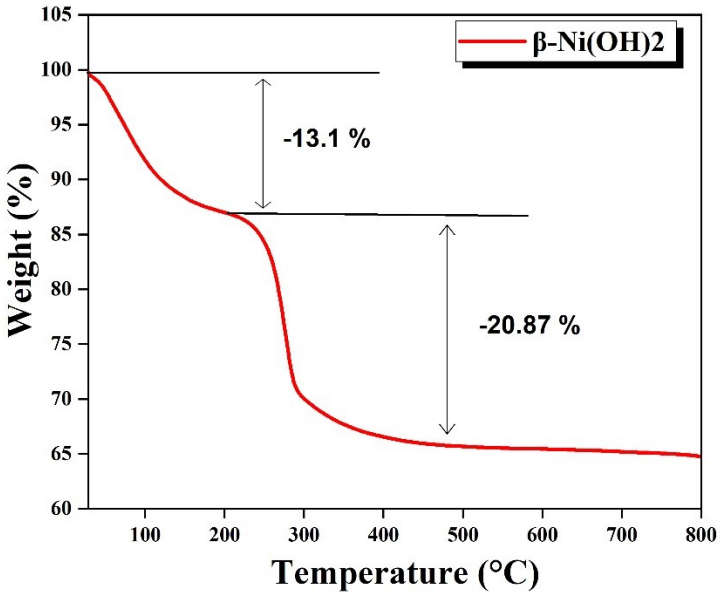

Figure S9. TGA graph of end-of-life LIB-derived **β-Ni(OH)$_2$**

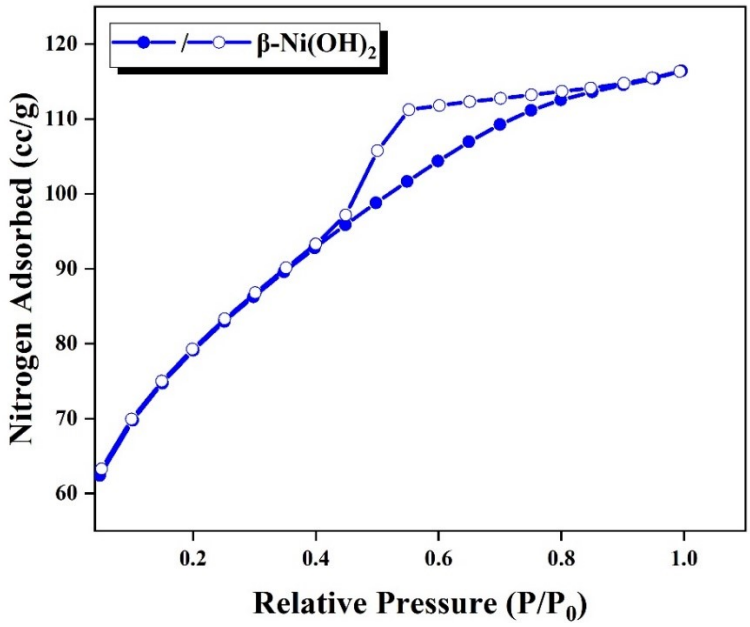

Figure S10. N_2 adsorption-desorption isotherm of end-of-life LIB-derived **β-Ni(OH)$_2$**

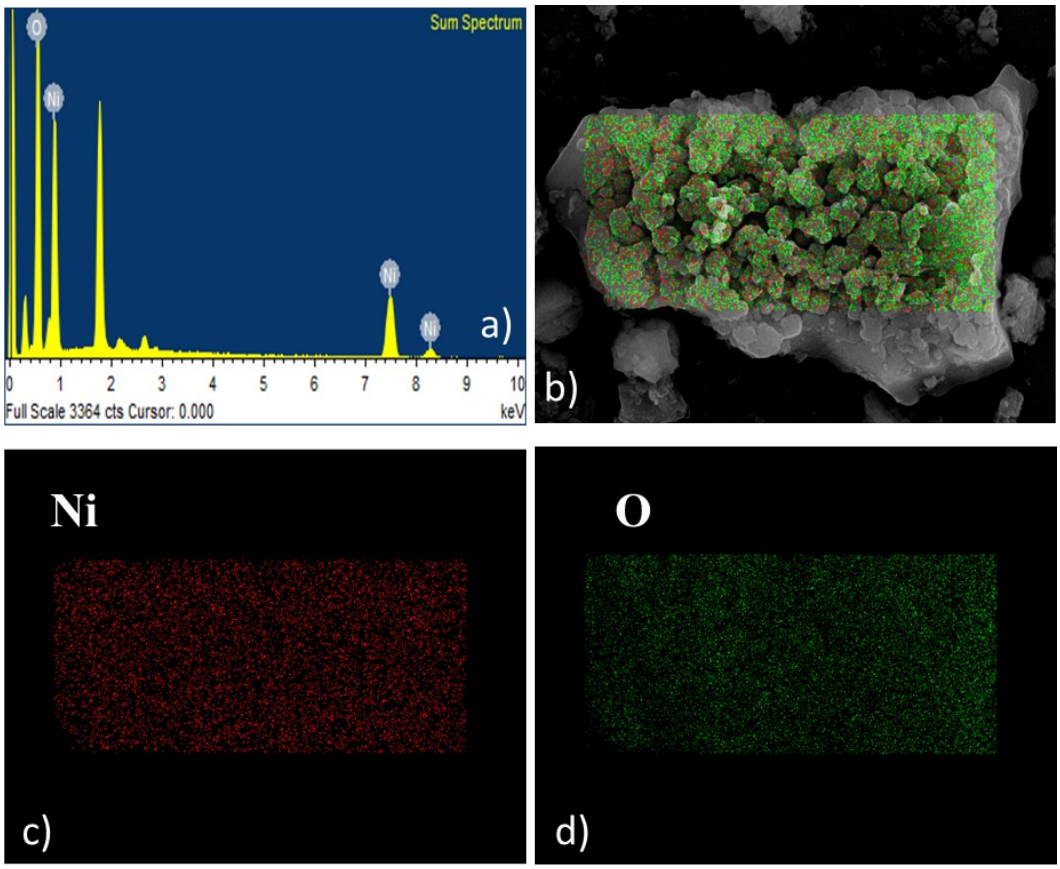

Figure S11. a) SEM-EDX of **β-Ni(OH)$_2$** showing the presence of elements Ni and O. FESEM elemental mapping of **β-Ni(OH)$_2$** is presented in b) – d), where b) represents the merged data of the elements while c) and d) elemental mapping of Ni and O respectively.

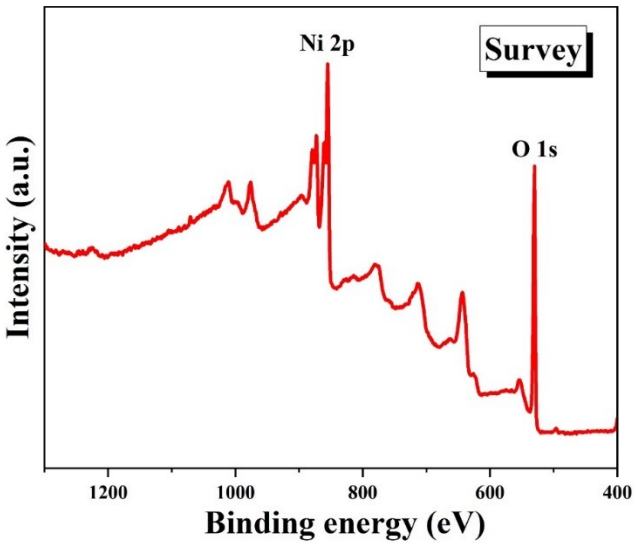

Figure S12. XPS survey spectrum of **β-Ni(OH)$_2$**.

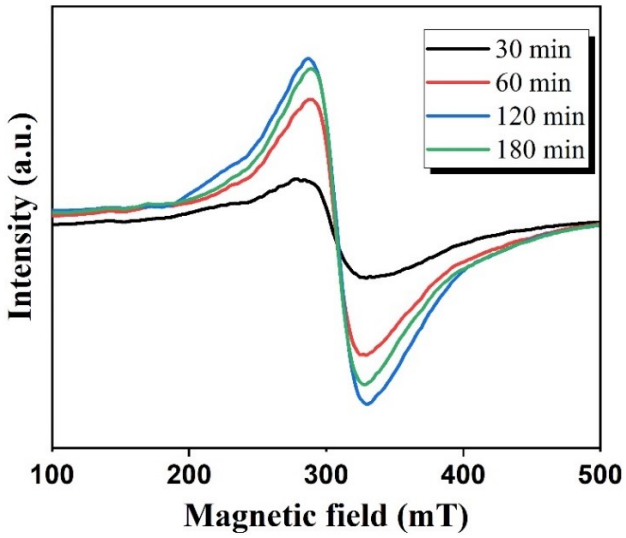

Figure S13. Ageing time dependent EPR spectra of **β-Ni(OH)$_2$.**

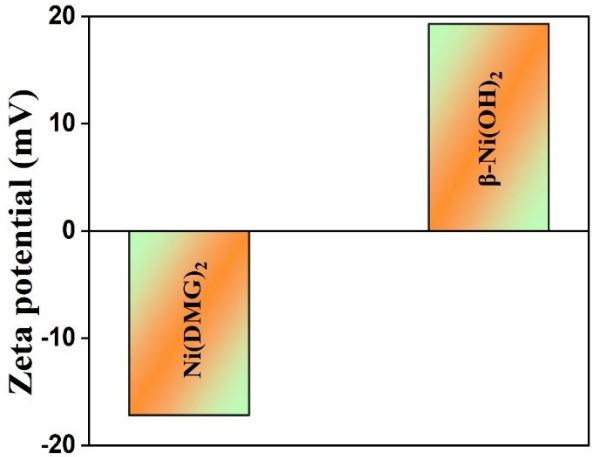

Figure S14. Surface potential values of **Ni(DMG)$_2$** and **β-Ni(OH)$_2$** respectively.

Table S1. Surface area and surface potential of $Ni(DMG)_2$ and β-$Ni(OH)_2$.

Sr.no.	Electrocatalyst	BET Surface area (m^2/g)	Pore size (nm)	Zeta potential (mV)
1	$Ni(DMG)_2$	12.11	2.76	-17.2
2	β-$Ni(OH)_2$	279.45	0.75	19.3

Table S2. ICP analysis of $Ni(DMG)_2$ and β-$Ni(OH)_2$ to determine the Ni loading in the materials.

Sr.no.	Electrocatalyst	ICP-MS (mg) (in 10 mg)
1	$Ni(DMG)_2$	1.56
2	β-$Ni(OH)_2$	3.12

3. Electrocatalytic OER:

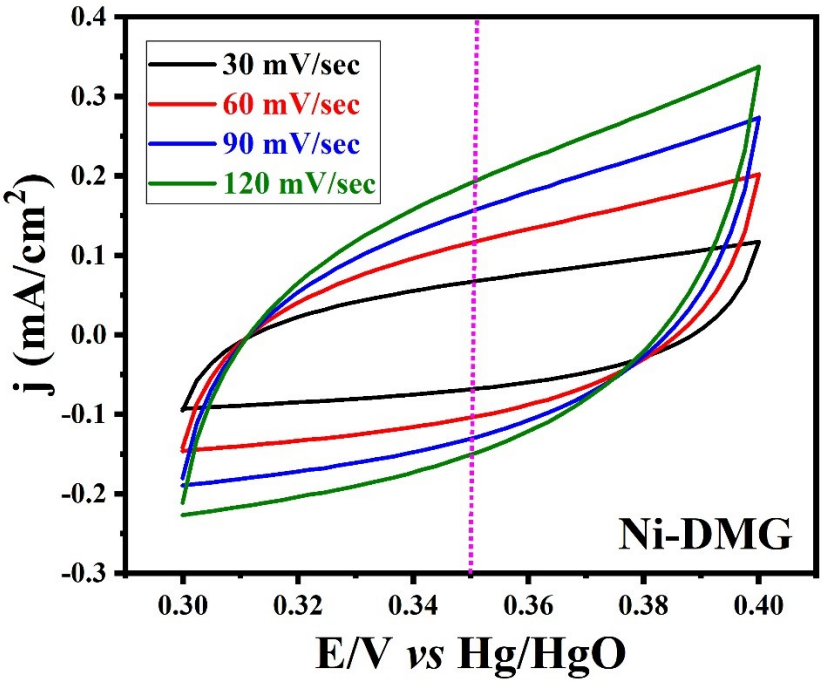

Figure S15. Double layer capacitance in the chosen region of non-Faradaic region for $Ni(DMG)_2$.

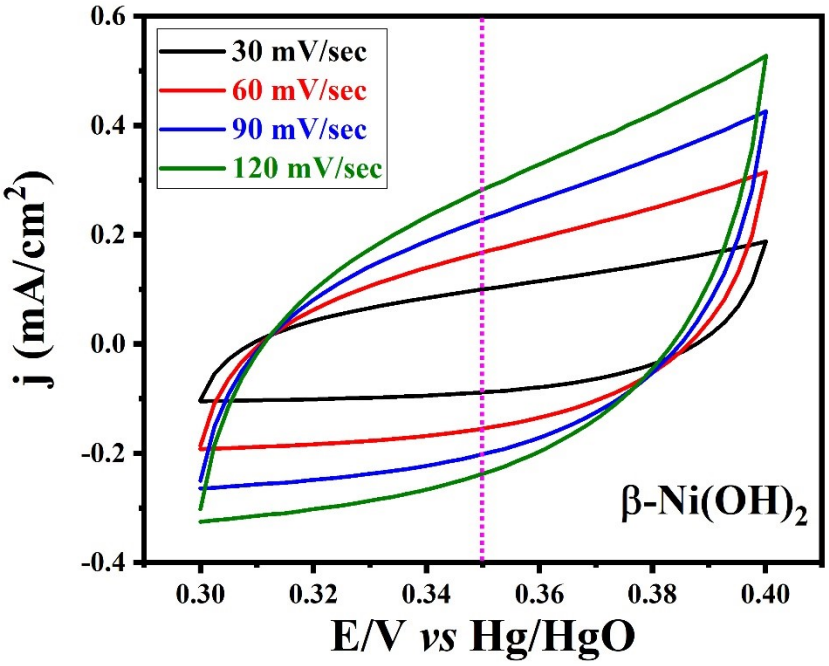

Figure S16. Double layer capacitance in the chosen region of non-Faradaic region for β-$Ni(OH)_2$.

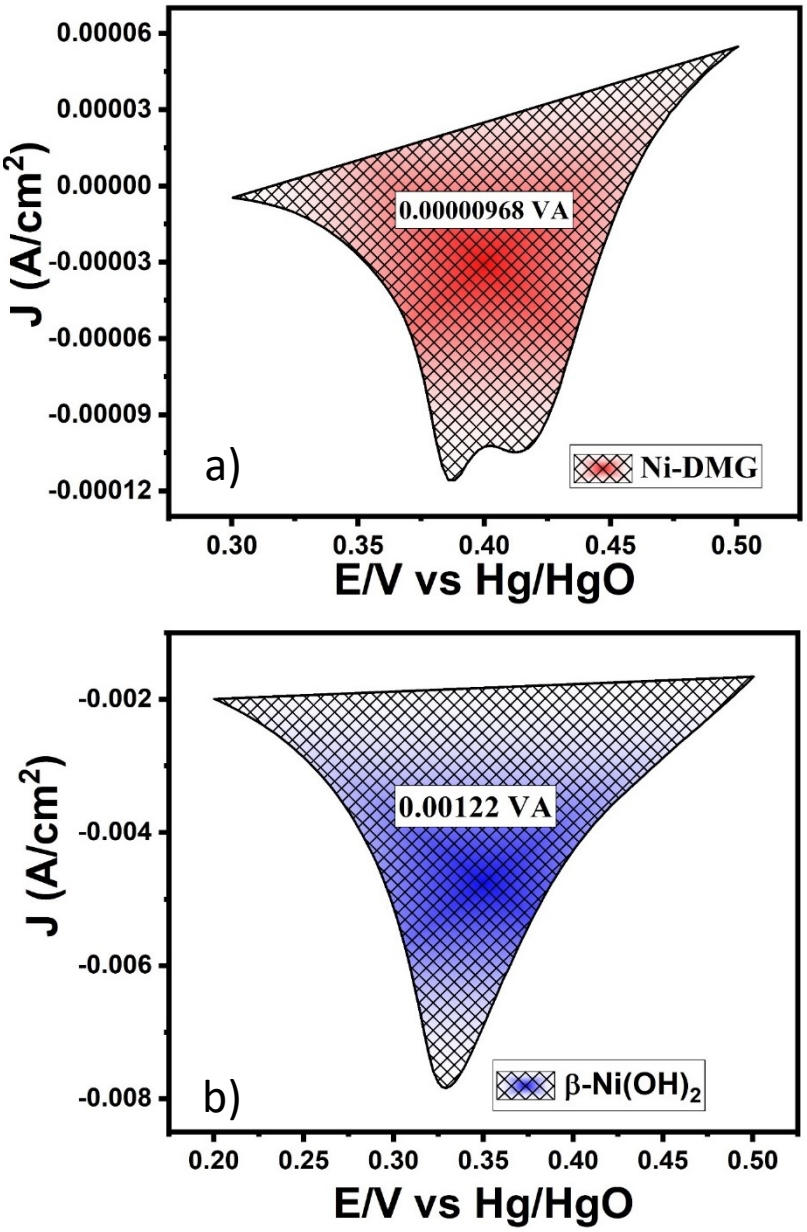

Figure S17: Reduction surface area for **Ni-DMG** and **β-Ni(OH)$_2$**.

4. Post-OER characterizations

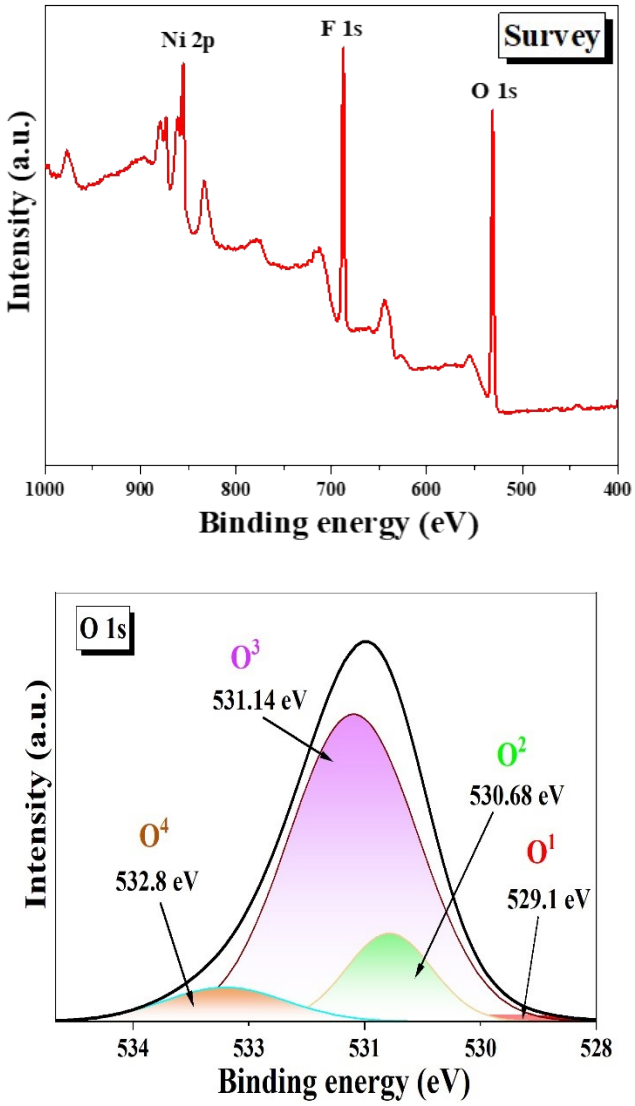

Figure S18. XPS Survey spectrum (upper panel) and O 1s XPS spectrum (bottom panel) of post-OER **β-Ni(OH)$_2$** catalyst.

TOF calculation:

The details procedure of the calculation of turnover frequency (TOF) has discussed below:

The per-site TOF value was calculated according to the following equation:

$$\text{TOF} = \left(\frac{total\ oxygen\ \ turnovers/cm^2}{active\ sites\ density}\right)$$

The number of total oxygen turnovers,

$$\text{TON} = (\text{j mA/cm}^2)\left(\frac{1\ C/s}{1000\ mA}\right)\left(\frac{1\ mol\ e^-}{96845.3\ C}\right)\left(\frac{1\ mol}{4\ e^-}\right)\left(\frac{6.023\ \times\ 10^{23}\ molecules\ of\ O_2}{1\ mol\ of\ O_2}\right)$$

The number of total oxygen turnovers was calculated from the current density extracted from the LSV polarization curve.

According to this, the number of total oxygen turnovers for 0.1 mg of catalyst loading would be

$$\text{TON}_{1.5\ \text{V}}\ (\beta\text{-Ni(OH)}_2) = (13.1\ \text{mA/cm}^2)\left(\frac{1\ C/s}{1000\ mA}\right)\left(\frac{1\ mol\ e^-}{96485\ C}\right)\left(\frac{1\ mol}{4\ e^-}\right)\left(\frac{6.023\ \times\ 10^{23}\ molecules\ of\ O_2}{1\ mol\ of\ O_2}\right) = 2.04 \times 10^{16}$$

$$\text{TON}_{1.5\ \text{V}}\ (\text{Ni(DMG)}_2) = (0.021\ \text{mA/cm}^2)\left(\frac{1\ C/s}{1000\ mA}\right)\left(\frac{1\ mol\ e^-}{96485\ C}\right)\left(\frac{1\ mol}{4\ e^-}\right)\left(\frac{6.023\ \times\ 10^{23}\ molecules\ of\ O_2}{1\ mol\ of\ O_2}\right) = 3.27 \times 10^{13}$$

Using the number of total hydrogen turnovers, active site density, and electrochemically active surface area; we converted the current density from the LSV polarization curve into TOF, as:

$$TOF = \left(\frac{total\ oxygen\ \ turnovers/cm^2}{active\ sites\ \times ECSA}\right)$$

$$TOF(\beta\text{-}Ni(OH)_2) = \left(\frac{total\ oxygen\ \ turnovers/cm^2}{active\ sites\ \times ECSA}\right) = \left(\frac{2.04\ \times 10^{16}}{8.6\ \times 10^{14}\ \times 0.0922}\right) = 257.2\ \text{sec}^{-1}$$

$$TOF(Ni(DMG)_2) = \left(\frac{total\ oxygen\ \ turnovers/cm^2}{active\ sites\ \times ECSA}\right) = \left(\frac{3.27\ \times 10^{13}}{2.65\ \times 10^{15}\ \times 0.0585}\right) = 0.21\ \text{sec}^{-1}$$

Table S3. Comparison of the electrocatalytic OER efficiency with the reported $Ni(OH)_2$-based systems.

Sr. no.	Electrocatalyst	Electrolyte	Current density (mA cm^{-1})	Overpotential (mV) (1 M KOH)	Tafel slop (mV dec^{-1})	TOF (s^{-1})	Reference
1	NR-$Ni(OH)_2$	1 M KOH	10	162	72	0.012	3
2	β-$Ni(OH)_2$ nanoplates	1 M KOH	10	340	69	0.182	4
3	β-$Ni(OH)_2$ nanosheets	1 M KOH	10	326	65.5	-	5
4	β-$Ni(OH)_2$ nanoplates	0.1 M KOH	10	474	87	0.015	6
5	β-$Ni(OH)_2$	1 M KOH	18	550	-	-	7
6	β-$Ni(OH)_2$ nanosheets	0.1 M KOH	10	300	43	47.14	8
7	Fe/ β-$Ni(OH)_2$	0.1 M	10	260	32	-	9
8	Fe/ β-$Ni(OH)_2$	1 M KOH	10	219	53-57	-	10
9	β-$Ni(OH)_2$/SSM	1 M KOH	50	280	164	-	11
10	NiFe-OOH_{OV}	1 M KOH	50	330@50 mV	38	0.12	12
11	α- $Ni(OH)_2$	1 M KOH	10	260	78.6	0.16	13
12	Ir/NiOOH	1 M KOH	10	270	45.2	-	14

13	Fe-Ni(OOH)	1 M KOH	10	260	-	1.5	[15]
14*	β-$Ni(OH)_2$	1 M KOH	10	264	42.7	257.2	our work

References:

1 M. Rath, L. P. Behera, B. Dash, A. R. Sheik and K. Sanjay, *Hydrometallurgy*, 2018, **176**, 229–234.

2 X. Yang, Y. Zhang, Q. Meng, P. Dong, P. Ning and Q. Li, *RSC Adv.*, 2021, **11**, 268–277.

3 X. P. Wang, H. J. Wu, S. B. Xi, W. S. V. Lee, J. Zhang, Z. H. Wu, J. O. Wang, T. D. Hu, L. M. Liu, Y. Han, S. W. Chee, S. C. Ning, U. Mirsaidov, Z. B. Wang, Y. W. Zhang, A. Borgna, J. Wang, Y. H. Du, Z. G. Yu, S. J. Pennycook and J. M. Xue, *Energy Environ. Sci.*, 2020, **13**, 229–237.

4 N. Kim, D. Lim, Y. Choi, S. E. Shim and S.-H. Baeck, *Electrochim. Acta*, 2019, **324**, 134868.

5 C. Liao, Z. Xiao, N. Zhang, B. Liang, G. Chen, W. Wu, J. Pan, M. Liu, X.-R. Zheng, Q. Kang, X. Cao, X. Liu and R. Ma, *Chem. Commun.*, 2021, **57**, 9060–9063.

6 X. Zhou, Z. Xia, Z. Zhang, Y. Ma and Y. Qu, *J. Mater. Chem. A*, 2014, **2**, 11799–11806.

7 G. A. Snook, N. W. Duffy and A. G. Pandolfo, *J. Power Sources*, 2007, **168**, 513–521.

8 S. Anantharaj, P. E. Karthik and S. Kundu, *Catal. Sci. Technol.*, 2017, **7**, 882–893.

9 K. Zhu, H. Liu, M. Li, X. Li, J. Wang, X. Zhu and W. Yang, *J. Mater. Chem. A*, 2017, **5**, 7753–7758.

10 T. Kou, S. Wang, J. L. Hauser, M. Chen, S. R. J. Oliver, Y. Ye, J. Guo and Y. Li, *ACS Energy Lett.*, 2019, **4**, 622–628.

11 A. A. Kashale, A. V. Ghule and I. P. Chen, *ChemCatChem*, 2021, **13**, 1165–1174.

12 Z. Ahmed, Krishankant, R. Rai, R. Kumar, T. Maruyama, C. Bera and V. Bagchi, *ACS Appl. Mater. Interfaces*, 2021, **13**, 55281–55291.

13 C. Luan, G. Liu, Y. Liu, L. Yu, Y. Wang, Y. Xiao, H. Qiao, X. Dai and X. Zhang, *ACS Nano*, 2018, **12**, 3875–3885.

14 J. Liu, J. Xiao, Z. Wang, H. Yuan, Z. Lu, B. Luo, E. Tian and G. I. N. Waterhouse, *ACS Catal.*, 2021, **11**, 5386–5395.

15 F. Dionigi and P. Strasser, *Adv. Energy Mater.*, 2016, **6**, 1600621.